Nano Research

Open Access

Research Article

Unveiling crystalline silicon edge subsurface passivation impact on photovoltaics via three-dimensional spatially resolved micro-photoelectrical mapping

Tianyu Lan[1], Jingsheng Jin[2], Wei Cui[2], Jiangtao Li[1], Jie Yang[2], Yusheng Wang[1] ✉, Xinyu Zhang[2], and Baoquan Sun[1,3] ✉

[1] State Key Laboratory of Bioinspired Interfacial Materials Science, Institute of Functional Nano & Soft Materials (FUNSOM), Soochow University, Suzhou 215123, China
[2] Research and Development (R & D) Department, Zhejiang Jinko Solar Co., Ltd., Haining 314416, China
[3] Macau Institute of Materials Science and Engineering (MIMSE), MUST-SUDA Joint Research Center for Advanced Functional Materials, Macau University of Science and Technology, Taipa, Macau 999078, China

Cite this article: *Nano Research*, **2026**, *19*, 94908354. https://doi.org/10.26599/NR.2026.94908354

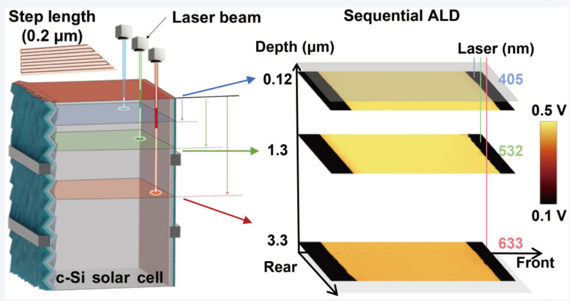

ABSTRACT: Employing half-cut thermal-laser-separation (TLS)-induced crystalline silicon (c-Si) wafers in high-efficiency solar cells is indispensable to mitigate cell-to-module (CTM) efficiency loss, which incurs unnecessary electrical loss due to the associated extra wafer edge. Atomic layer deposition (ALD) AlO_x films are widely used to passivate edge defects arising from CTM loss in c-Si photovoltaic (PV) modules. However, the inferior spatial resolution and the absence of depth perception inherent in current photoelectric characterization technologies fail to disclose the passivation properties of AlO_x films fabricated by diverse ALD processes, hindering further development to address edge electrical defects. Here, a high spatial resolution (up to ~ 0.3 μm) three-dimensional multi-laser integration system was developed to investigate the impact of TLS-induced edge recombination on c-Si solar cells. The results show that sequential ALD AlO_x films offer superior passivation, especially for subsurface defects. The process improved the power conversion efficiency of a large-scale PV module (2278 mm × 1134 mm) from 22.95% to 23.17%, an increase of 0.22%. Further elemental analysis confirmed the subsurface passivation effects, including the enhanced hydrogen diffusion and an enlarged surface electric field. This work provides critical insights into edge defects in industrial c-Si solar cells, guiding the optimization of ALD-based edge passivation.

KEYWORDS: silicon solar cells, three-dimensional (3D) photoelectrical imaging, subsurface passivation, AlO_x films

1 Introduction

Crystalline silicon (c-Si) solar cells incorporating passivating contacts have recently experienced substantial advancements [1]. In particular, tunnel oxide passivating contact (TOPCon) solar cells have become the mainstream in the current market due to their high efficiency and process compatibility [2]. Although the record power conversion efficiency (PCE) of TOPCon solar cells has reached 26.58% [3], the module PCE cannot reach such a high value due to cell-to-module (CTM) losses. Commercial module efficiencies generally fall short of cell efficiencies by approximately 2.5% due to the CTM loss [4]. Assembling a photovoltaic (PV) module series–parallel interconnection configuration from half-cut cells can significantly reduce CTM loss while increasing output power. Furthermore, the half-cell separation process enhances the wafer fabrication throughput for mass production and lowers manufacturing costs [5]. However, cutting solar cells into modules disrupts their crystal structure, creating dangling bonds at the exposed edges that act as recombination centers, reducing the minority-carrier lifetime and the overall PCE of the modules [6]. Specifically, the TOPCon cells could suffer an edge recombination loss of 0.5% based on the modeling of an M0 cell [7]. Moreover, for high-efficiency TOPCon solar cells, the edge recombination has a greater effect on absolute efficiency losses after cutting than for lower-efficiency solar cells. Consequently, the technology of half-cell

Received: October 3, 2025; **Revised:** November 22, 2025
Accepted: December 17, 2025

✉Address correspondence to Yusheng Wang, yushengwang@suda.edu.cn; Baoquan Sun, bqsun@suda.edu.cn

separation has experienced rapid advancement, among which the thermal-laser-separation (TLS) technology has been widely applied [8]. Although optimized TLS techniques can significantly reduce the electrical losses in CTM, cutting still induces a large number of edge defects.

In this context, the edge defect passivation has emerged as a hot topic, as it can recover lost PCE and even enhance PCE in solar modules [9]. Generally, applying the atomic layer deposition (ALD) technology to deposit dielectric films (such as AlO_x, SiO_x, and SiN_x) on the cell surface can effectively passivate the surface defects, thereby mitigating the formation of recombination centers [10–12]. The passivation effect of dielectric films relies on chemical passivation and field effect passivation. On the one hand, dielectric films deposited via ALD exhibit high density, facilitating the formation of chemical bonds between silicon and the dielectric layers, thereby passivating silicon dangling bonds at the silicon surface [13]. On the other hand, the inherent high dielectric constant of dielectric films enables the formation of a dielectric layer with a significant negative fixed interface charge density, thereby contributing to the physical passivation of defects via the field-effect mechanism [14]. Research has demonstrated that employing ALD to deposit dielectric films on the edges of silicon wafers can effectively mitigate the recombination losses induced by edge defects, leading to substantial improvements in the photovoltaic performance of c-Si solar cells [15]. Specifically, the deposition of dielectric films has been shown to reduce carrier recombination at the cut edges, thus improving parameters such as photocurrent, open-circuit voltage (V_{OC}), and fill factor (FF) [16]. Furthermore, the combination of process optimization and various ALD techniques has proven beneficial in enhancing the quality of the passivation layer, increasing the cell efficiency, and incresing the module output power [17, 18]. These ALD processes are categorized into sequential and spatial. Sequential ALD, the conventional method, introduces precursors sequentially, with purge steps in between to prevent mixing, thereby limiting deposition rate and throughput [19]. Spatial ALD, an improvement over sequential ALD, continuously delivers precursors to separate reaction zones as the substrate moves between them [20]. Eliminating purge steps increases the deposition rate and efficiency, making spatial ALD more suitable for large-scale production.

However, recent research has predominantly focused on improving efficiency through edge-defect passivation using various materials [19–22], with insufficient emphasis on quantitative investigation of edge-defect distribution and recombination pathways. Electroluminescence (EL) imaging, a well-established traditional defect characterization technique, can provide rapid, non-destructive diagnostics of PV devices with micrometer-scale spatial resolution (more than 10 μm) [23]. However, the current state of EL imaging technology is constrained by its limited spatial resolution and the absence of depth perception, which impede the investigation of edge defect distribution and the comprehensive disclosure of AlO_x passivation properties. As a result, novel optoelectrical characterizations should be conducted to explore the edge defect states of c-Si solar cells and to screen potential materials and suitable deposition technologies for half-cell edge passivation.

Here, a high-resolution three-dimensional (3D) photocurrent/photovoltage micro-area characterization system was used to investigate the edge-defect distribution and its impact on the photovoltaic performance of TOPCon solar cells at a submicron scale. To facilitate this, we used three lasers with varying penetration depths to acquire optoelectrical mapping across different depth sections. First, we analyzed carrier diffusion transport with edge defects in c-Si solar cells using spatial photocurrent distribution. To facilitate this, spatial ALD and sequential ALD techniques were used to fabricate half-cell samples cut by TLS technology. After that, the photovoltage mapping with different depths was conducted in the cross-section to explain the excellent defect passivation by the sequential ALD AlO_x thin film. Further characterization confirmed that sequential ALD enhanced both the chemical and field-effect passivation of superficial and inner defects. Notably, in combination with cross-section photovoltage mapping, our findings indicate that TLS cutting induces a vertical distribution of surface and subsurface defects along the cell edges, which cannot be resolved by conventional characterization techniques. Therefore, our work sheds light on the multidimensional characterization and elucidates the subsurface passivation mechanisms that can guide the optimization of industrial ALD processes.

2 Results and discussion

2.1 Edge defects passivated by ALD AlO_x thin film

To explore the physical mechanism of edge-defect passivation using AlO_x films, we prepared three sets of samples. All three sets were based on high-efficiency TOPCon cells that were cut into half-cells using TLS technology. Sample 1 referred to the cut cell that was not coated with any film. Sample 2 was passivated with a thin AlO_x film deposited via spatial ALD after cutting, denoted as spatial ALD. Sample 3 was passivated with AlO_x using sequential ALD deposition after cutting, denoted as sequential ALD. The front and rear side photographs of these three samples are shown in Fig. S1 in the Electronic Supplementary Material (ESM). The output power and PCE of the modules for these samples are shown in Fig. S2 in the ESM. Here, the reference sample after the TLS method cutting has an average power output of 593 W with an average PCE of 22.95%. After depositing AlO_x thin film using spatial ALD and sequential ALD methods, the output power increased to 597.3 and 598.7 W, respectively. Meanwhile, the PCE of these modules increased to 23.12% and 23.17%, respectively. In addition to the module-level performance, Figure S3 in the ESM presents the J–V characteristics of 2 cm × 2 cm cells taken from the same samples. The detailed photovoltaic parameters, V_{OC}, short-circuit current density (J_{SC}), FF, and PCE of all tested cells are summarized in Table S1 in the ESM. The uncoated sample shows the lowest V_{OC}, FF, and PCE due to severe recombination at the damaged edge. Both ALD-passivated samples exhibit improved device parameters, with the sequential ALD sample achieving the highest overall performance, consistent with its superior edge-passivation capability. To explore the reason behind these differences, we carried out photocurrent and photovoltage mapping along and perpendicular to the cutting surface. The schematic diagram for testing photocurrent/photovoltage is shown in Fig. 1(a). A laser spot is directed from the cut edge of the cell and scanned point by point into the interior, yielding a high-resolution distribution of photocurrent/photovoltage. The photocurrent-mapping images in Fig. 1(b) show the photocurrent distribution on both the front and rear sides of the cells.

Due to inherent variations between the cells, we normalized the photocurrent distributions with the raw data shown in Fig. S4 in the ESM. It should also be noted that, for more precise

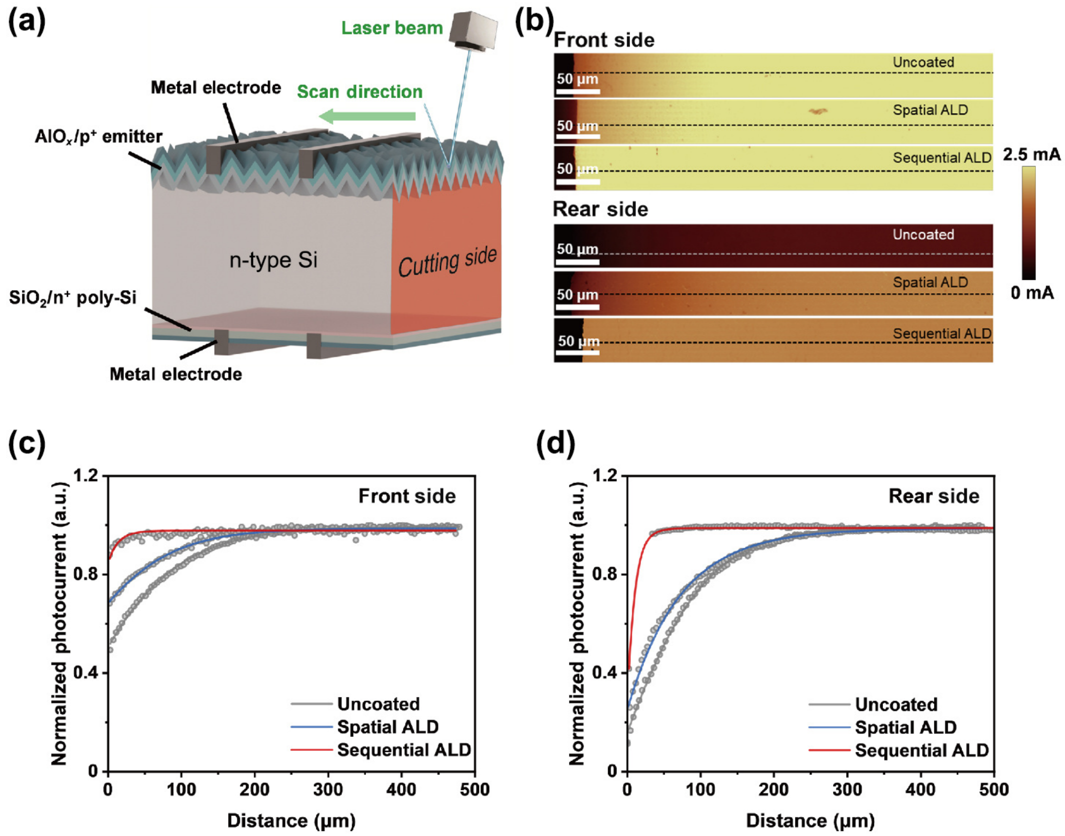

Figure 1 High spatial resolution photocurrent and photovoltage mapping based on a micro-photocurrent/photovoltage imaging system. (a) Schematic diagram illustrating photocurrent and photovoltage mapping, showing the structure of edge-cutting TOPCon solar cells. (b) Spatially resolved photocurrent distributions along the edges of the front and rear sides of TOPCon solar cells are shown for three different processing treatments: uncoated, spatial ALD AlO_x layer at the edge, and sequential ALD AlO_x layer at the edge. (c) and (d) Normalized photocurrent distribution collected from (b) along the cross-sectional image lines at the cell edge.

visualization, the datasets used in Figs. 1(c) and 1(d) were down-sampled by selecting one point every 20 data points during plotting. Further observations in Figs. 1(c) and 1(d) reveal significant differences in the photocurrent distribution from the edge to the interior after different treatments. It is assumed that, without passivation, severe recombination occurs at the edge (x = 0), resulting in very low photocurrent values. After passivation, the photocurrent at the edge shows an increasing trend, with sequential AlO_x providing better passivation performance. Additionally, the rear-side photocurrent was clearly lower than that on the front, with edge losses more pronounced. As we know, the TOPCon solar cell is an asymmetric structure. The front side features a textured anti-reflection structure, resulting in a higher photocurrent value on the front surface. In addition, by accounting for losses due to cutting on the different faces of the c-Si solar cell, we conclude that recombination losses are more severe on the rear side, which is likely the n$^+$ polysilicon region. Further analysis of the longitudinal recombination of solar cells will be discussed below.

To further analyze the photocurrent distribution, we constructed a simplified one-dimensional model of lateral charge transport for the c-Si solar cell. Considering the simplified one-dimensional case, the laser irradiates the cell at x_0, generating the corresponding photo-generated minority carriers, Δp_{x_0}. The photo-generated carriers diffuse to both sides. On the one side, as distance x tends to infinity, we assume that the carrier concentration at infinity is zero.

$$\Delta p(x = x_0) = \Delta p_{x_0} \tag{1}$$

$$\Delta p(x = \infty) = 0 \tag{2}$$

On the other side, at x = 0, we assume that a recombination center exists with an edge recombination velocity S_P.

$$\Delta p(x = x_0) = \Delta p_{x_0} \tag{3}$$

$$D_P \frac{\mathrm{d}\Delta p(x)}{\mathrm{d}x}(x = 0) = S_P \cdot \Delta p_{x_0} \tag{4}$$

These boundary conditions were introduced into the diffusion equation.

$$D_P \frac{\mathrm{d}^2 \Delta p}{\mathrm{d}x^2} = \frac{\Delta p}{\tau} \tag{5}$$

Finally, integrating from x = 0 to ∞, we obtained the charge generated by the laser at $x = x_0$.

$$q(x_0) = \int_0^\infty e \cdot p(x)\mathrm{d}x \tag{6}$$

The photocurrent was proportional to the collected charge.

$$I(x_0) = \frac{k \cdot \left\{\left[L_R \cdot D_P \cdot \sinh\left(\frac{x_0}{L_R}\right) + L_R^2 \cdot S_P \cdot \cosh\left(\frac{x_0}{L_R}\right) - L_R^2 \cdot S_P\right]\right\}}{D_P \cdot \cosh\left(\frac{x_0}{L_R}\right) + L_R \cdot S_P \cdot \sinh\left(\frac{x_0}{L_R}\right)} \tag{7}$$

where k is the proportional coefficient, L_P is the diffusion length, D_P is the diffusion coefficient, S_P is the recombination velocity, and L_R is the recombination length.

Using the derived equation to fit the experimental photocurrent distribution, we obtained the data shown in Table S2 in the ESM. L_R and S_P for each of the three samples were obtained. Firstly, the edge recombination length of the uncoated sample is 67.5 μm, while the edge recombination lengths of the samples passivated with spatial and sequential AlO_x are 54.7 and 29.1 μm, respectively. On the other hand, regarding the recombination rate, the original edge recombination rate is 11,000 cm/s, which decreases to 7000 and 3000 cm/s after passivation with spatial and sequential AlO_x, respectively. L_R reflects the distance over which edge defects influence lateral charge transport, while S_P is related to the density of defect states at the edge [24]. From the derived data, it was clear that after passivation with AlO_x, the edge defect state density decreased significantly, and internal carrier recombination was reduced. Furthermore, it was seen that, for both the recombination velocity and recombination length, the spatial AlO_x passivation was notably inferior to the sequential AlO_x passivation. To correlate the locally extracted recombination parameters with the overall photovoltaic response, we measured the external quantum efficiency (EQE) spectra of three representative cells at both the inner and edge regions (Fig. S5 in the ESM). The inner region was used as the reference, as it is considered to be well passivated. The unpassivated edge exhibits a pronounced EQE loss across the entire spectral range, consistent with the considerable recombination length and high recombination velocity obtained from the lateral photocurrent analysis. After the AlO_x passivation, both spatial and sequential ALD samples show a clear broadband enhancement in edge EQE, with the sequential ALD sample demonstrating the most substantial improvement. These results verify that the increase in current density arises from the effective suppression of edge-induced recombination rather than wavelength-dependent optical effects, providing experimental support for the theoretical parameters extracted from the spatially resolved photocurrent distribution. Although we successfully extracted two key physical parameters from the spatially-resolved photocurrent distribution using the diffusion equation, we aimed to verify these theoretical results through experimental analysis.

2.2 Longitudinal carrier transport mechanism

It is worth noting that our theoretical analysis assumes that edge defects are concentrated on the cutting surfaces. Given the differences in defect distribution along the direction perpendicular to the cutting surface of the c-Si cells, we conducted a detailed photoelectrical analysis on the cells' side surfaces. Although our equipment is capable of performing photocurrent and photovoltage imaging tests, photovoltage is more sensitive to defects at the device interface [25]. Therefore, for the photoelectrical testing at the lateral interfaces, we chose the photovoltage mapping as the characterization method. The test schematic is shown in Fig. 2(a), where three lasers are used to scan the c-Si cross-section from the rear to the front of the TOPCon solar cell, enabling the study of the vertical charge-transport mechanism. n-TOPCon cells feature an asymmetric structure, with a textured p^+ emitter on the front side and a polished n^+ polysilicon doped layer on the rear side. We also used three sets of samples for this analysis and established a simplified physical model, as shown in Fig. 2(b). We assumed that the distribution of defect states has a depth difference. Here, we have four different situations after cutting using the TLS method. Since cutting is performed on the surface, a substantial number of defect states are inevitably present there. Thus, the defect concentration will decrease with depth because the inner wafer is in a low-defect state. Actually, the uncoated surface formed after cutting by the TLS method is coated with a thin oxide layer, known as native passivation, which passivates a few surface defects to some extent [26]. However, we hypothesized that the TLS cutting process influences the defect concentration in the direction perpendicular to the cutting surface. The surface defect states decrease while more defects remain inside. Therefore, the defect concentration will increase to a peak due to insufficient inner passivation. In addition, after defect passivation by spatial and sequential ALD AlO_x thin film, the surface defect concentration will decrease due to the dense film, and subsurface defects will be passivated by both chemical and field effect passivation simultaneously. Ultimately, due to differences between the two methods, inner defects in sequential ALD samples can be passivated more effectively than in spatial ALD. Because we used n-type TOPCon cells as samples (Fig. 2(c)), when the laser irradiates the n-region, the minority-carrier holes must diffuse and drift over a considerable distance. The cutting process increased the recombination probability, leading to a substantial decline in charge collection. As a result, there was severe photovoltage loss near the n^+ polysilicon layer. The specific data are shown in Figs. 2(d)–2(f). Using cross-sectional line scans, we obtained high spatial resolution photovoltage distributions. The original data cross-section photovoltage distribution is shown in Fig. S6 in the ESM. However, the values for different samples and the powers of different lasers differ slightly. Furthermore, because laser power varies, we tested the photovoltage distribution under different laser powers, as shown in Fig. S7 in the ESM. Although the photovoltage grows with increasing power, its distribution is independent of laser power. Therefore, we normalized the subsequent photovoltage distribution for comparison with those obtained using different lasers. To maintain visual clarity in the vertical profiles, the datasets used in Figs. 2(g)–2(i) were also down-sampled by selecting one point every 20 data points during plotting. From Figs. 2(g)–2(i), the vertical photovoltage distributions after different treatments are visible.

Overall, we observed that the photovoltage in the n^+ polysilicon layer was significantly lower than in the p^+ emitter region, and after passivation, the difference was reduced. Moreover, the photovoltage distribution trends varied under different lasers, especially with the 633 nm laser, where the photovoltage was much lower than under the other two lasers. For the uncoated cells, the photovoltage under 405 nm laser excitation in the n^+ polysilicon region was almost identical to that under 532 nm laser excitation. In contrast, under 633 nm laser excitation, it decreased significantly in the same region. Additionally, to clarify the operating principles of our multi-wavelength photovoltage mapping, it should be noted that the three excitation lasers used (405, 532, and 633 nm) correspond to penetration depths of approximately 0.12, 1.3, and 3.3 μm in c-Si, respectively (Fig. S8 in the ESM) [27]. This enables depth-resolved photovoltage imaging, which can be further integrated into a 3D photovoltage distribution. Here, we observed that under 633 nm laser excitation, subsurface defects were detected, as reflected in lower photovoltage values compared to the surface. Therefore, we speculated that, for uncoated cells, the surface had only a thin silicon oxide passivation layer, which was ineffective in our model. Based on our physical model, it was inferred that cutting would not only generate a large number of defects on the cell surface but also incur severe subsurface and even deeper defects, leading to recombination within the cell. In addition, after passivation by

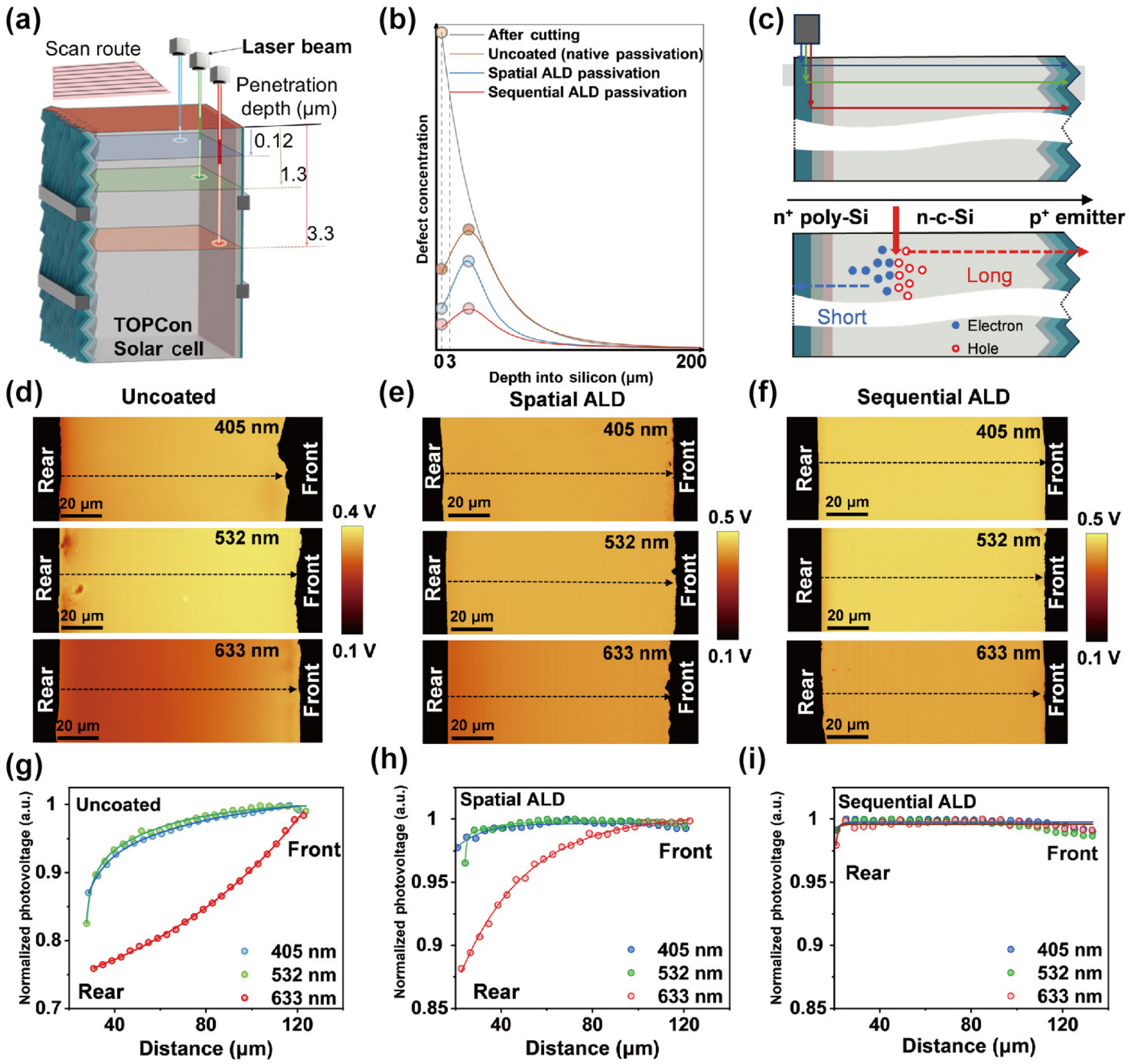

Figure 2 Spatially resolved photovoltage distributions caused by different edge defects of TOPCon solar cells with various processing treatments after cutting. (a) Schematic of the test setup, where three pulsed lasers with various penetration depths illuminate the TOPCon solar cells with three different edge processing treatments. (b) Defect concentration distribution perpendicular to the cutting side in different samples. (c) Schematic diagram of charge separation in the TOPCon solar cell model after laser irradiation. 3D spatially resolved photovoltage images under three lasers for each treatment condition: (d) uncoated, (e) spatial ALD AlO_x layer at the edge, and (f) sequential ALD AlO_x layer at the edge. (g)–(i) show the spatially resolved normalized photovoltage distributions collected from ((d)–(f)) along the cross-sectional image lines of the TOPCon solar cell.

spatial AlO_x, the photovoltage in both the n^+ and p^+ regions becomes nearly identical under both 405 and 532 nm lasers. However, under 633 nm laser excitation, cells passivated with spatial AlO_x showed a reduced photovoltage distribution in the n^+ polysilicon region. We deduced that this AlO_x did not effectively passivate subsurface defect states in these samples. In contrast, samples passivated with sequential AlO_x exhibited nearly identical photovoltage distribution trends under all three lasers, indicating excellent passivation of subsurface defects by sequential AlO_x. What's more, these observed differences were confirmed not to arise from wavelength-dependent responses of the c-Si solar cell to lasers of varying powers. For instance, heterojunction structures exhibit significant parasitic absorption, while edge-transparent conductive oxide layers demonstrate notable ultraviolet attenuation [28]. To verify that the photovoltage loss was due to the defect-state distribution caused by cutting, rather than differences in laser wavelengths, we performed non-destructive separation by cutting along the crystal direction on TOPCon cells and measured the photovoltage distribution under different lasers, as shown in Fig. S9 in the ESM. The photovoltage distributions under three types of lasers exhibited the same trend.

In cross-sectional photovoltage distribution studies, we found that edge defects generated after cutting had a depth distribution exceeding 3 μm perpendicular to the cutting surface. Moreover, the two ALD AlO_x films exhibited different passivation qualities for these depth-distributed defects. We will conduct a more in-depth analysis of the passivation differences between spatial ALD and sequential ALD.

2.3 Element diffusion at AlO_x/Si interface

Generally, the passivation quality of AlO_x depends on both chemical and field-effect passivation mechanisms [10]. We first analyzed the chemical passivation quality of the AlO_x films prepared using two different ALD processes. Employing transmission electron microscopy (TEM), we analyzed the AlO_x/Si interface in both samples, as illustrated in Fig. 3. Figures 3(a) and 3(e) display the interface details for spatial and sequential AlO_x films. The interface is generally divided into three parts: $AlO_x/SiO_2/Si$ [29]. We found that the thickness of AlO_x is approximately 40 nm, with no significant difference between the two samples. However, at the SiO_2/Si interface, we observed that the sequential AlO_x film appears to exhibit a diffusion trend. To further verify if element diffusion occurs in sequential AlO_x, we performed an energy dispersive X-ray spectroscopy (EDS) scan mapping on this region, as shown in Figs. 3(b) and 3(f). In the spatial AlO_x, the boundaries between Al, O, and Si were clearly visible. In contrast, in the sequential AlO_x, there was a diffusion trend of Al and O elements into the silicon layer. Moreover, the time-of-flight secondary ion mass spectrometry (TOF-SIMS) data further confirmed this, as shown in Figs. 3(c) and 3(g). The diffusion range of elements in spatial AlO_x was significantly smaller than that in sequential AlO_x. We deduced that these elements that diffuse into the interior serve a function in achieving deep passivation. A detailed analysis of the various elements is presented in Fig. S10 in the ESM. Here, the hydrogen element plays a crucial role in passivating edge defects [30]. In spatial AlO_x films, the hydrogen distribution was more uniform, while in sequential AlO_x, hydrogen accumulated significantly at the Al/Si interface. Based on the TOF-SIMS data of the H element, we illustrated the chemical passivation schematic model in Figs. 3(d) and 3(h). Here, hydrogen can effectively form Si–H bonds with silicon, reducing the density of the interface dangling bonds and decreasing surface defect concentration. Therefore, sequential AlO_x exhibits better chemical passivation at the interface [31]. Thus, we concluded that the interface after sequential AlO_x passivation had a lower interface defect density and a lower edge recombination rate, corresponding to better edge defect passivation.

2.4 Electrical field effect passivation at AlO_x/Si interface

To further analyze the electrical properties of these thin films, we used the Kelvin probe force microscopy (KPFM) characterization. The test schematic is shown in Fig. 4(a). We deposited a gold layer on the AlO_x film as a reference and measured the potential difference between the AlO_x and gold surfaces to determine the AlO_x film work function. The surface topographies of these two samples are shown in Fig. S11 in the ESM. As shown in Fig. 4(b), both AlO_x films showed a surface potential lower than that of gold, with the spatial AlO_x having a remarkably lower value. By extracting the cross-sectional line scan from Figs. 4(b) and 4(c), we observed that the spatial AlO_x has a significantly higher surface potential compared to the sequential AlO_x. By converting to contact potential difference (CPD) and work function values, as shown in Fig. 4(d) and Fig. S12 in the ESM, we found that the work function of sequential AlO_x is approximately 4.8 eV, whereas that of spatial AlO_x is only 4.3 eV, indicating a significant difference. The large difference in the work function of AlO_x is mainly due to the spatial charge differences formed at the AlO_x/Si interface [32]. We established a physical model, as shown in Fig. 4(e), to explain the differences. A substantial number of defect states existed at the interface between silicon and silicon oxide, which could not be completely passivated solely through chemical passivation. Therefore, the field effect passivation plays an indispensable role [33]. The fixed negative charge in AlO_x leads to band bending at the interface, as shown in Figs. 4(f) and 4(g). The difference in Al and O element diffusion at the interface results in a more negative surface charge in sequential AlO_x compared to spatial AlO_x. This makes the band bending in the n-silicon region more pronounced, forming a wider depletion region that shields charges and provides superior edge defect passivation. The field effect passivation schematic model is shown in Fig. S13 in the ESM. Although both spatial and sequential AlO_x can provide efficient chemical passivation, interface defects still remain. Here, sequential AlO_x,

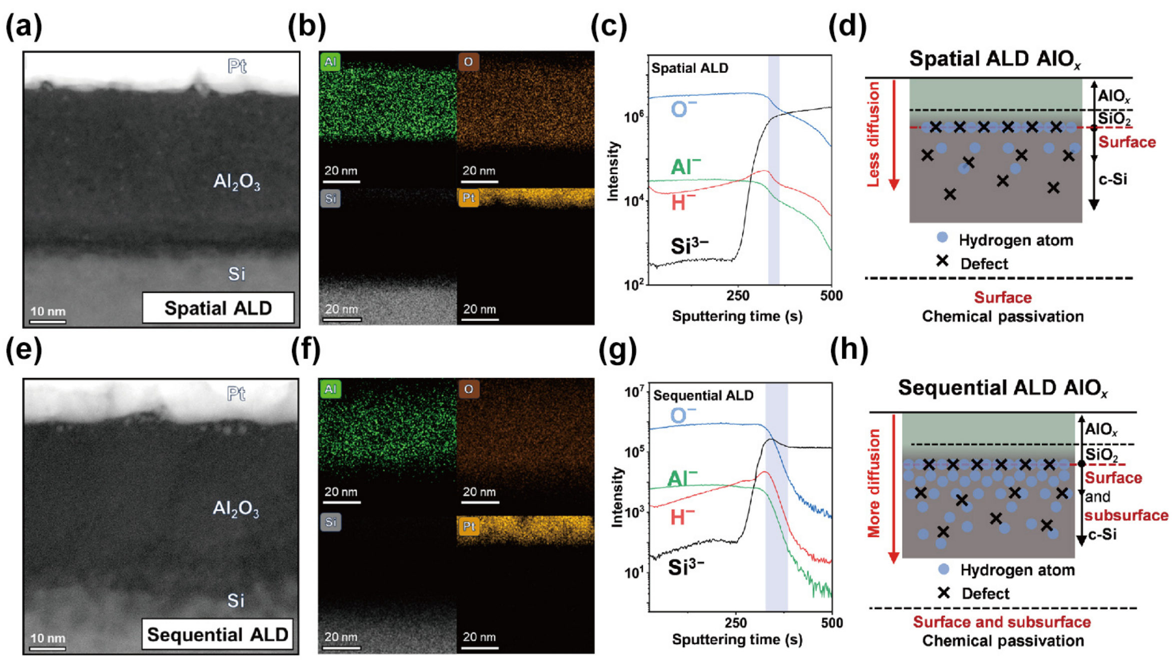

Figure 3 Cross-sectional element analysis of solar cells after edge coating passivation. TEM cross-section images for (a) spatial ALD AlO_x and (e) sequential ALD AlO_x. (b) and (f) Corresponding EDS mapping images for (a) and (e), respectively. Cross-sectional flight secondary ion mass spectrometry (TOF-SIMS) images: (c) spatial ALD AlO_x and (g) for sequential ALD AlO_x. Schematic model of chemical passivation for (d) spatial ALD AlO_x and (h) sequential ALD AlO_x.

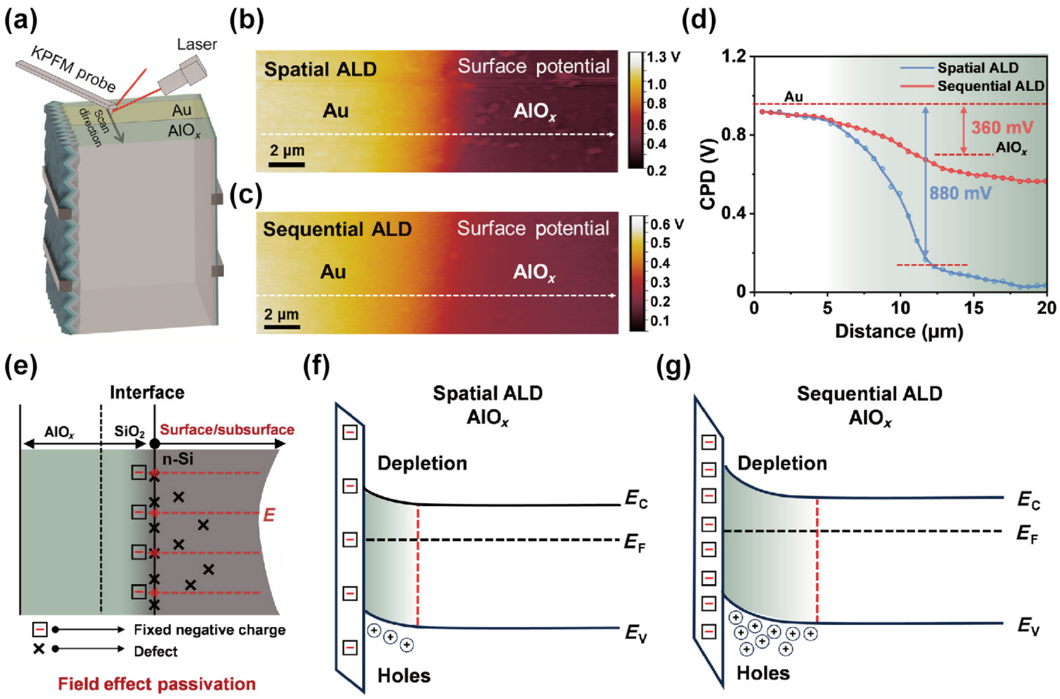

Figure 4 Electric analysis of edge defect passivation coating treatment on the edge of TOPCon solar cells. (a) Schematic diagram illustrating the test setup for KPFM measurement at the edge cross-section position. Surface potential distribution images of (b) spatial AlO_x and (c) sequential AlO_x. (d) Spatially resolved CPD distribution collected from (b) and (c) along the cross-section image lines. (e) The charges and defects distribution diagram is at the AlO_x/Si interface. (f) and (g) Band diagrams for the interfaces between spatial AlO_x/Si and sequential AlO_x/Si.

when applied at the edges, was very effective in passivating internal defects, whereas spatial AlO_x failed to effectively passivate subsurface and deeper defects. As illustrated in Fig. S12 in the ESM, significant differences exist between spatial ALD and sequential ALD processes. As we mentioned before, spatial ALD reconfigures the sequential precursor separation into a geometric arrangement, continuously delivering precursors to separate reaction zones as the substrate moves between them [34]. This approach effectively isolates the potential interactions between distinct gases and the occurrence of half-reactions. It is postulated that this isolation leads to a sharper interface in the deposited thin films, thereby significantly mitigating atomic diffusion. Nevertheless, appropriate diffusion in this situation is not inferior, which makes a distinct inner passivation. Owing to its high throughput and lower cost, spatial ALD has been widely adopted for edge passivation in industrial c-Si solar modules. Our results, therefore, indicate that suitably engineered post-treatments are crucial for further improving the performance of spatial ALD AlO_x films, particularly in passivating deeper defect states beneath the c-Si edge.

3 Conclusions

In summary, we developed a high-resolution (up to ~ 0.3 μm) 3D method for quantitative characterization of edge defects in c-Si solar cells. We applied this technology to investigate the physical mechanism of edge-defect passivation using AlO_x films. In comparison with the uncoated sample, which had a cutting efficiency of 22.95%, samples with spatial ALD and sequential ALD showed increases to 23.12% and 23.17%, respectively. By quantitatively extracting the recombination length and recombination velocity from the photocurrent mapping, we quantified the spatial impact of the edge defect. In addition, the three-dimensional and high-spatial-resolution photoelectrical characterization enables us to study the submicrometer passivation effect via photovoltage mapping at different laser penetration depths. We found that surface, subsurface, and even deeper silicon suffered significant optoelectrical losses. Further results showed that sequential ALD exhibited the best overall defect passivation, with superior inner defect passivation. This passivation mechanism was verified by sufficient chemical passivation from element diffusion and field effect passivation from fixed charge density. Overall, this work provides important insights into multidimensional microscale characterization and advanced edge passivation strategies, offering guidance for the design and optimization of ALD processes to minimize edge-related losses in high-efficiency c-Si solar cells and modules.

4 Experimental methods

4.1 Samples

The TOPCon solar cells were provided by Jinko Solar Co., Ltd. The layers, from top to bottom, comprised an Ag finger contact, a SiN_x antireflection and passivating layer, a p^+ emitter layer, an n-type c-Si layer, a SiO_2 tunnel layer, an n^+ polysilicon layer, and a SiN_x antireflection layer, all of which were covered by an Ag finger contact. All three sample types were processed based on these TOPCon solar cells, which were cut into half-cells using TLS technology and passivated using different ALD methods.

4.2 Photovoltage/photocurrent mapping instrumentation

The photocurrent/photo-voltage mapping system was developed based on the WITec α300R confocal Raman imaging system and performed *XY* two-dimensional photovoltage/photocurrent mapping. The excitation sources were 405, 532, and 633 nm lasers. Coupled with a 50× objective, the optical system achieved a spot diameter of ~ 1 μm, providing the highest spatial resolution of ~ 0.3 μm required for imaging over the *X*-axis (*Y*-axis). To obtain the photocurrent and photovoltage mapping images, a 50 μm × 500 μm region was mapped using a 250 × 2500 grid. In addition, the longitudinal photovoltage cross-sectional areas were characterized using a 50× objective and 187,500 data points, with region sizes of 50 μm × 150 μm. A laser power of 10 mW was set unless specified.

4.3 Elemental and electrical characterization

The TEM sample was fabricated using the focused ion beam (FIB) lift-out technique to characterize the AlO_x/Si contact cross-section. High-angle annular dark-field (HAADF) images of scanning TEM (STEM) coupled with EDS mappings were acquired using a FEI Talos F200X. TOF-SIMS depth profile was performed using a 30 keV Bi^{3+} primary ion beam alternating with a 1 keV Cs^+ sputtering ion beam to get the element depth profiles of Si, Al, H, and O. The surface potential of the AlO_x/Au sample was determined using KPFM measurements (Bruker-MultiMode). The *J*–*V* characteristics of solar cells were determined by a solar simulator (SS-X100-R) at a simulated AM 1.5G and under illumination at 1000 W/m^2 and 25 °C. The EQE was tested using an integrated EQE test system (QE-R in Enli Technology Co., Ltd.) in whole surface light mode.

Electronic Supplementary Material: Supplementary material (photographs of three samples; module output power and PCE metrics; raw spatial maps of photocurrent and photovoltage; penetration depths in c-Si for lasers of different wavelengths; TOF-SIMS depth profiles of H, O, and Al; AFM topography, CPD, and work-function measurements comparing two ALD samples; schematic field-effect passivation models contrasting spatial and sequential AlO_x; process schematics for both ALD deposition modes; and a summary table reports recombination length L_R and surface recombination velocity S_P) is available in the online version of this article at https://doi.org/10.26599/NR.2025.94908354.

Data availability

All data needed to support the conclusions in the paper are presented in the manuscript and the Electronic Supplementary Material. Additional data related to this paper may be requested from the corresponding author upon request.

Acknowledgements

This work was granted by the National Key Research and Development Program of China (No. 2023YFB4202600).

Declaration of competing interest

All the contributing authors report no conflict of interests in this work.

Author contribution statement

T. Y. L.: Data curation, investigation, methodology, visualization, writing – original draft, writing – review & editing. J. S. J.: Formal analysis, investigation, methodology, resources, software, writing – original draft. W. C.: Investigation, methodology, project administration, software. J. T. L.: Investigation, methodology, visualization. J. Y.: Funding acquisition, project administration, supervision, validation. Y. S. W.: Investigation, methodology, project administration, writing – original draft, writing – review & editing. X. Y. Z.: Supervision, resources, project administration. B. Q. S.: Funding acquisition, methodology, project administration, supervision, writing – review & editing. All the authors have approved the final manuscript.

Use of AI statement

None.

References

[1] Melskens, J.; van de Loo, B. W. H.; Macco, B.; Black, L. E.; Smit, S.; Kessels, W. M. M. Passivating contacts for crystalline silicon solar cells: From concepts and materials to prospects. *IEEE J. Photovolt.* **2018**, *8*, 373–388.

[2] IEA. *Trends in Photovoltaic Applications 2024* [Online]. IEA: Paris, France, 2024. https://iea-pvps.org/wp-content/uploads/2024/10/IEA-PVPS-Task-1-Trends-Report-2024.pdf (accessed Feb 20, 2025).

[3] Trinasolar. *Trinasolar Announces Efficiency of 26.58% for n-type TOPCon Cells, Setting the 28th World Record* [Online]. Trinasolar: Changzhou, China, 2024. https://static.trinasolar.com/en-apac/resources/newsroom/aptrinasolar-announces-efficiency-2658-n-type-topcon-cells-setting-28th-world (accessed Feb 20, 2025).

[4] Ballif, C.; Haug, F. J.; Boccard, M.; Verlinden, P. J.; Hahn, G. Status and perspectives of crystalline silicon photovoltaics in research and industry. *Nat. Rev. Mater.* **2022**, *7*, 597–616.

[5] Guo, S. Y.; Schneider, J.; Lu, F.; Hanifi, H.; Turek, M.; Dyrba, M.; Peters, I. M. Investigation of the short-circuit current increase for PV modules using halved silicon wafer solar cells. *Sol. Energy Mater. Sol. Cells* **2015**, *133*, 240–247.

[6] Xu, G. J.; Yan, K.; Wang, L.; Lv, S.; Ma, A. N.; Li, J.; Qing, A. A comparative experimental study on front and back laser cutting technology for mass separation of N-TOPCon crystal silicon solar cells. *Sol. Energy Mater. Sol. Cells* **2024**, *271*, 112844.

[7] Fell, A.; Schön, J.; Müller, M.; Wohrle, N.; Schubert, M. C.; Glunz, S. W. Modeling edge recombination in silicon solar cells. *IEEE J. Photovolt.* **2018**, *8*, 428–434.

[8] Martel, B.; Albaric, M.; Harrison, S.; Dhainaut, F.; Desrues, T. Addressing separation and edge passivation challenges for high efficiency shingle heterojunction solar cells. *Sol. Energy Mater. Sol. Cells* **2023**, *250*, 112095.

[9] Baliozian, P.; Al-Akash, M.; Lohmüller, E.; Richter, A.; Fellmeth, T.; Munzer, A.; Wohrle, N.; Saint-Cast, P.; Stolzenburg, H.; Spribille, A. et al. Postmetallization "passivated edge technology" for separated silicon solar cells. *IEEE J. Photovolt.* **2020**, *10*, 390–397.

[10] Dingemans, G.; Kessels, W. M. M. Status and prospects of Al_2O_3-based surface passivation schemes for silicon solar cells. *J. Vac. Sci. Technol. A* **2012**, *30*, 040802.

[11] Reichel, C.; Feldmann, F.; Richter, A.; Benick, J.; Hermle, M.; Glunz, S. W. Polysilicon contact structures for silicon solar cells using atomic layer deposited oxides and nitrides as ultra-thin dielectric interlayers. *Prog. Photovoltaics: Res. Appl.* **2022**, *30*, 288–299.

[12] Gao, K.; Xu, D. C.; Wang, J.; Bi, Q. Y.; Wu, Z.; Lin, H.; Wang, S. B.; Shi, W.; Yu, C.; Cao, F. X. et al. Efficient silicon solar cells with aluminum-doped zinc oxide-based passivating contact. *Adv. Funct. Mater.* **2025**, *35*, 2415039.

[13] Girisch, R. B. M.; Mertens, R. P.; De Keersmaecker, R. F. Determination of Si–SiO_2 interface recombination parameters using a gate-controlled point-junction diode under illumination. *IEEE Trans. Electron Devices* **1988**, *35*, 203–222.

[14] Aberle, A. G.; Glunz, S.; Warta, W. Field effect passivation of high efficiency silicon solar cells. *Sol. Energy Mater. Sol. Cells,* **1993**, *29*, 175–182.

[15] Weber, J.; Kniffki, L.; Gutmann, L.; Huyeng, J.; Lohmüller, E.; Rößler, T. Investigating the impact of edge passivation on shingle solar modules. *Sol. Energy Mater. Sol. Cells,* **2024**, *271*, 112876.

[16] Wang, X.; Zhang, X. N.; Bai, Y. H.; Li, W. H.; Chen, B. B.; Guo, J. X.; Yang, X. L.; Yan, X. B.; Wang, S. F.; Chen, J. H. Development of passivating edge shingle modules with right cut, new loss evaluation and liquid-based edge passivation strategy. *Sol. Energy Mater. Sol. Cells,* **2023**, *261*, 112513.

[17] Li, W. K.; Zhou, R.; Wang, Y. K.; Su, Q. F.; Yang, J.; Xi, M.; Liu, Y. S. Preparation of Al_2O_3 thin films by RS-ALD and edge passivation application for TOPCon half solar cells. *Appl. Surf. Sci.* **2024**, *673*, 160835.

[18] Lohmüller, E.; Baliozian, P.; Gutmann, L.; Kniffki, L.; Beladiya, V.; Geng, J.; Wang, L. L.; Dunbar, R.; Lepert, A.; Hofmann, M. et al. Thermal laser separation and high-throughput layer deposition for edge passivation for TOPCon shingle solar cells. *Sol. Energy Mater. Sol. Cells* **2023**, *258*, 112419.

[19] Dingemans, G.; Seguin, R.; Engelhart, P.; Sanden, M. C. M. V. D.; Kessels, W. M. M. Silicon surface passivation by ultrathin Al_2O_3 films synthesized by thermal and plasma atomic layer deposition. *Phys. Status Solidi-Rapid Res. Lett.* **2010**, *4*, 10–12.

[20] Poodt, P.; Cameron, D. C.; Dickey, E.; George, S. M.; Kuznetsov, V.; Parsons, G. N.; Roozeboom, F.; Sundaram, G.; Vermeer, A. Spatial atomic layer deposition: A route towards further industrialization of atomic layer deposition. *J. Vac. Sci. Technol. A* **2012**, *30*, 010802.

[21] Li, W. H.; Wang, X.; Guo, J. X.; Zhang, X. N.; Chen, B. B.; Chen, J. W.; Gao, Q.; Yang, X. L.; Li, F.; Wang, J. M. et al. Compensating cutting losses by passivation solution for industry upgradation of TOPCon and SHJ solar cells. *Adv. Energy Sustain. Res.* **2023**, *4*, 2200154.

[22] Chen, N.; Tune, D.; Buchholz, F.; Roescu, R.; Zeman, M.; Isabella, O.; Mihailetchi, V. D. Stable passivation of cut edges in encapsulated n-type silicon solar cells using Nafion polymer. *Sol. Energy Mater. Sol. Cells* **2023**, *258*, 112401.

[23] Chen, B. Y.; Peng, J.; Shen, H. P.; Duong, T.; Walter, D.; Johnston, S.; Al-Jassim, M. M.; Weber, K. J.; White, T. P.; Catchpole, K. R. et al. Imaging spatial variations of optical bandgaps in perovskite solar cells. *Adv. Energy Mater.* **2019**, *9*, 1802790.

[24] deQuilettes, D. W.; Yoo, J. J.; Brenes, R.; Kosasih, F. U.; Laitz, M.; Dou, B. D.; Graham, D. J.; Ho, K.; Shi, Y. W.; Shin, S. S. et al. Reduced recombination via tunable surface fields in perovskite thin films. *Nat. Energy* **2024**, *9*, 457–466.

[25] Qiu, J. M.; Mei, X. Y.; Zhang, M. X.; Wang, G. L.; Zou, S. W.; Wen, L.; Huang, J. M.; Hua, Y.; Zhang, X. L. Dipolar chemical bridge induced $CsPbI_3$ perovskite solar cells with 21.86% efficiency. *Angew. Chem., Int. Ed.* **2024**, *63*, e202401751.

[26] Chowdhury, Z. R.; Cho, K.; Kherani, N. P. High-quality surface passivation of silicon using native oxide and silicon nitride layers. *Appl. Phys. Lett.* **2012**, *101*, 021601.

[27] Polyanskiy, M. N. Refractiveindex. info database of optical constants. *Sci. Data* **2024**, *11*, 94.

[28] Wen, L. L.; Zhao, L.; Wang, G. H.; Jia, X. J.; Xu, X. H.; Qu, S. Y.; Li, X. T.; Zhang, X. Y.; Xin, K.; Xiao, J. H. et al. Beyond 25% efficient crystalline silicon heterojunction solar cells with hydrogenated amorphous silicon oxide stacked passivation layers for rear emitter. *Sol. Energy Mater. Sol. Cells* **2023**, *258*, 112429.

[29] Hoex, B.; Heil, S. B. S.; Langereis, E.; van de Sanden, M. C. M.; Kessels, W. M. M. Ultralow surface recombination of *c*-Si substrates passivated by plasma-assisted atomic layer deposited Al_2O_3. *Appl. Phys. Lett.* **2006**, *89*, 042112.

[30] Dingemans, G.; Beyer, W.; van de Sanden, M. C. M.; Kessels, W. M. M. Hydrogen induced passivation of Si interfaces by Al_2O_3 films and SiO_2/Al_2O_3 stacks. *Appl. Phys. Lett.* **2010**, *97*, 152106.

[31] Schön, J.; Hamer, P.; Hammann, B.; Zechner, C.; Kwapil, W.; Schubert, M. C. Hydrogen in silicon solar cells: The role of diffusion. *Sol. RRL* **2025**, *9*, 2400668.

[32] Song, W. J.; Yoshitake, M. A work function study of ultra-thin alumina formation on NiAl (110) surface. *Appl. Surf. Sci.* **2005**, *251*, 14–18.

[33] Bonilla, R. S.; Hoex, B.; Hamer, P.; Wilshaw, P. R. Dielectric surface passivation for silicon solar cells: A review. *Phys. Status Solidi (A)* **2017**, *214*, 1700293.

[34] Hoffmann, L.; Theirich, D.; Pack, S.; Kocak, F.; Schlamm, D.; Hasselmann, T.; Fahl, H.; Räupke, A.; Gargouri, H.; Riedl, T. Gas diffusion barriers prepared by spatial atmospheric pressure plasma enhanced ALD. *ACS Appl. Mater. Interfaces* **2017**, *9*, 4171–4176.